Quantum scattering of hot H/D on CO_2: Cross sections and rate coefficients for planetary atmospheres and their evolution

Cheikh T. Bop[1] & Marko Gacesa[1,2]⋆

[1] *Physics Department, Khalifa University, Abu Dhabi, United Arab Emirates*
[2] *Khalifa University Space Technology & Innovation Laboratory, Khalifa University, Abu Dhabi, United Arab Emirates*

ABSTRACT

Collisions between hot hydrogen atoms and CO_2 play a central role in energy transfer and atmospheric escape in CO_2-rich planetary atmospheres. We present quantum mechanical j_z-conserving coupled-states calculations of state-resolved cross sections for H/D–CO_2 collisions at energies up to 5 eV, benchmarked to within 7% of close-coupling results. Scattering is strongly forward-peaked, yielding momentum-transfer cross sections substantially smaller than commonly assumed: mass-scaling from O/C–CO_2 systems overestimates H–CO_2 total cross sections by factors of 30–45, while existing empirical fits underestimate the low-energy regime by up to ∼45%. Isotopic substitution (H/D) produces energy-dependent differences of up to 35% at $E < 0.1$ eV, invalidating uniform scaling approaches for D/H fractionation. Maxwellian-averaged rate coefficients derived from our cross sections are significantly smaller than mass-scaled values, implying reduced H–CO_2 energy transfer efficiency. In atmospheric escape modelling, these revisions can shift Martian exobase altitudes by 10–20 km, leading to order-unity changes in thermal escape rates, and have implications for hydrogen loss in early CO_2-dominated planetary atmospheres. Our results provide essential quantum-mechanical inputs for revisiting atmospheric evolution scenarios on Mars, early Earth, and CO_2-rich exoplanets.

Key words: planets and satellites: atmospheres – molecular data – molecular processes

1 INTRODUCTION

Carbon dioxide (CO_2) is among the most abundant molecules in planetary, cometary, and exoplanetary atmospheres (Feaga et al. 2007; Limaye et al. 2018; Madhusudhan 2012; Turbet et al. 2018; Cadieux et al. 2024), including temperate terrestrial worlds like TRAPPIST-1e and LHS 1140 b where it may dominate atmospheric composition. Its large moment of inertia and high atmospheric abundance make CO_2 a dominant collision partner in the upper atmospheres of terrestrial planets, where it governs radiative cooling and mediates energy exchange with suprathermal atoms.

Modelling hydrogen escape from CO_2-rich atmospheres has historically relied on simplified collisional treatments dating back to foundational work by Hunten (1973) and Schunk & Nagy (1980), which employ hard-sphere or isotropic scattering approximations. These approaches underpinned the development of hydrodynamic escape theory and its application to mass fractionation of noble gases during the 'flight of the nobility' and water loss from terrestrial planets (Zahnle & Kasting 1986; Zahnle et al. 1990). However, these classical approximations do not capture the quantum-mechanical details of light-atom–molecule collisions — particularly the strongly forward-peaked scattering that characterizes H/D–CO_2 interactions. In the absence of system-specific data, modern studies often resort to reduced-mass scaling or surrogate systems (Lewkow & Kharchenko 2014; Gacesa et al. 2020), despite evidence that such approximations can introduce order-of-magnitude errors in transport cross sections. Moreover, for light atoms colliding with heavy polyatomic targets, quantum diffraction and interference dominate the angular distribution, rendering classical or isotropic approximations particularly unreliable.

On Mars, where CO_2 constitutes over 95% of the present atmosphere (Jakosky et al. 2017), these uncertainties propagate directly into atmospheric escape and isotopic fractionation calculations. Photochemical production of energetic H atoms drives long-term water loss and surface oxidation (Jakosky et al. 2018; Gregory et al. 2023b), creating a substantial suprathermal population capable of escaping from the upper thermosphere (Amerstorfer et al. 2017; Fox & Hać 2009; Fox 2015). These atoms arise primarily from dissociative recombination of ions such as HCO^+ (Fox & Hać 2009; Gregory et al. 2023a). Observations reveal strong seasonal and solar-cycle modulation of hydrogen escape (Chaffin et al. 2014; Mayyasi et al. 2023; Susarla et al. 2024), linked to perihelion heating, water transport, and exobase H densities. Crucially, MAVEN data show that escape of both H and D is controlled not only by thermal processes but also by a persistent suprathermal component (Clarke et al. 2024; Lillis et al. 2017). A purely thermal escape rate for D is nearly two orders of magnitude too small to explain the observed upper-

atmospheric D/H variations. In this regime, isotopic fractionation becomes highly sensitive to the efficiency of momentum and energy loss through collisions with CO_2, making accurate elastic and rotationally inelastic H/D–CO_2 cross sections essential for interpreting modern D/H ratios in terms of long-term water loss. Recent photochemical models confirm that deuterium escape requires a significant non-thermal component (Cangi et al. 2023), and isotopic evolution studies show that preferential escape of lighter isotopes controls the modern isotopic composition of the Martian atmosphere (Thomas et al. 2023). In the upper thermosphere, suprathermal H and D atoms experience only a handful of collisions, so the assumed elastic and momentum-transfer cross sections directly govern escape probabilities and D/H fractionation (Gregory et al. 2023a; Chaufray et al. 2024).

Here we present new quantum mechanical calculations of state-to-state, total, and differential cross sections for rotationally elastic and inelastic collisions of H and D atoms with CO_2 at collision energies up to 5 eV. These results provide essential inputs for modelling suprathermal energy transfer, hydrogen and deuterium escape, and isotopic evolution in CO_2-rich planetary atmospheres. Section 2 describes the computational approach, Section 3 presents the results and discussion, and Section 4 summarizes the main conclusions.

## 2 COMPUTATIONAL DETAILS

2.1 Potential energy surface

The interaction between H and rigid-rotor CO_2 is described by the high-level *ab initio* potential energy surface (PES) of Dagdigian (2015). The PES was computed using the coupled-cluster method RCCSD(T) with an augmented quadruple-zeta basis set and includes corrections for basis-set superposition error. We employ the same PES for both H–CO_2 and D–CO_2 systems, as the Born–Oppenheimer interaction depends only on nuclear coordinates and is invariant under isotopic substitution. For details of the PES construction and its contour plots, we refer the reader to the original paper (Dagdigian 2015).

2.2 Cross sections

We implemented the radial coefficients (V_λ) of the H-CO_2 PES, made available by Dagdigian (2015), in the `MOLSCAT` computer code (Hutson & Green 1994). The long-range part ($R \geq 28\ a_0$) of these coefficients was derived by extrapolation using the following inverse power law (Ndaw et al. 2021; Bop & Lique 2023):

$$V_\lambda(R) = \frac{C_\lambda}{R^{\eta_\lambda}}. \qquad (1)$$

The parameters C_λ and η_λ were retrieved using the radial coefficients corresponding to the last *ab initio* points to ensure a gradual descent of the potentials. The scattering processes of interest in this study can be described as

$$CO_2(j) + H/D \quad \rightarrow \quad CO_2(j') + H/D, \qquad (2)$$
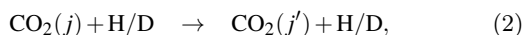
where j denotes the rotational quantum number of CO_2. Since the projectiles have kinetic energies reaching up to 5 eV, we employed the quantum mechanical j_z-conserving coupled states (CS) approximation (McGuire & Kouri 1974),

combined with the hybrid log-derivative-Airy propagator of Alexander & Manolopoulos (1987), to solve the scattering problem. The CS method offers significant computational savings compared to the fully rigorous close-coupling (CC) approach (Alexander 1977) and remains accurate at suprathermal collision energies, typically above $\sim$0.1–0.2 eV (Gong et al. 2025).

The scattering calculations were performed for total energies up to $E = 5$ eV. To derive highly accurate collision data, we performed prior convergence tests. The rotational basis was set large enough, including the 141 low-lying energy levels for CO_2, i.e. $j = 0 - 140$. The integration boundaries, $R_{\min}$ and $R_{\max}$, were automatically adjusted for each total angular momentum (J) of the collision systems H-CO_2 and D-CO_2. We used up to 241 partial waves, i.e. $J = 0 - 240$, to achieve convergence of both elastic and inelastic cross sections. The parameter `STEPS`, which is interpreted as the number of steps per half-wavelength for the open channel of highest kinetic energy in the asymptotic region, was set to 30 for $E \leq 1$ eV and 10 for total energies up to 5 eV. All these parameters ensure the subpercent convergence of high-magnitude state-to-state cross sections ($\geq 10^{-2}\ \mathring{A}^2$). The low-magnitude collision data have very minor effect on the total cross sections, and their subpercent convergence requires an extremely large rotational basis ($j = 0 - 350$), which is computationally challenging due to memory limitations and CPU times.

Scope and limitations. The present calculations treat CO_2 as a linear rigid rotor with fixed bond lengths, so vibrational excitation and vibration–rotation coupling are neglected. This approximation is suitable for the cross sections presented here because, over the energy range considered, vibrational excitation mainly redistributes energy into internal degrees of freedom of CO_2 and is expected to have a sub-dominant effect on the momentum-transfer cross sections most relevant to atmospheric escape.

The interaction is described by a single ground-state Born–Oppenheimer potential energy surface, so electronic excitation and non-adiabatic effects are not included. Finally, most scattering calculations employ the j_z-conserving coupledstates approximation rather than full close coupling; based on the benchmark in Fig. 4, the resulting transport cross sections are accurate to within $\sim$7% over the energy range considered, but the CS approximation may be less reliable very near threshold and for subtle interference features in differential cross sections. We also neglect reactive channels and treat the collisions as non-reactive scattering on a single PES; the results are intended for energy and momentum transfer in atmospheric-transport contexts rather than chemical kinetics, and earlier studies of reactive scattering involving $O(^3P)$ and H_2 at suprathermal energies reported reactive cross sections at least two orders of magnitude smaller than for non-reactive channels (Balakrishnan 2004; Garton et al. 2003; Gacesa & Kharchenko 2014; Gacesa et al. 2017).

3 RESULTS AND DISCUSSION

3.1 Integral and differential cross sections

Fig. 1 shows the state-to-state cross sections $\sigma_{j=0 \to j'}$ for selected collision energies, representative of translationally hot
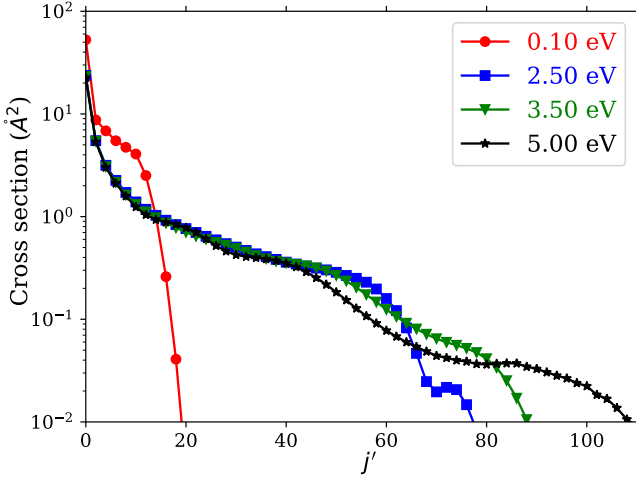
**Figure 1.** State-to-state cross sections $\sigma_{j=0\to j'}$ for the scattering of CO_2 with H for selected collision energies.

H atoms colliding with thermal CO_2. Throughout this section, collision energies are expressed in the centre-of-mass frame unless stated otherwise. The contribution of inelastic transitions decreases rapidly with increasing j'. At all energies considered, the largest Δj transitions are up to four orders of magnitude smaller than the elastic channel and up to three orders of magnitude smaller than the dominant inelastic transitions. Transitions to $j' > 140$, which are not included in this work, therefore contribute negligibly to the total cross section $\sigma_{j=0}^{tot}$.

In Fig. 2 we compare total cross sections $\sigma_{j=0}^{tot}$ for CO_2 in collisions with different projectiles for kinetic energies up to 5 eV. As seen in the lower panel, the H–CO_2 and D–CO_2 cross sections follow similar energy-dependent trends, with differences decreasing as the kinetic energy increases. At $E \leq 0.1$ eV, D-induced cross sections exceed those from H by up to $\sim 35\%$, whereas for $E > 0.1$ eV the difference falls below 9%. This reflects the longer de Broglie wavelength and greater quantum diffractive scattering for the lighter H projectile at low energies. For both isotopes, elastic scattering accounts for 40-55% of the total cross section across the full energy range.

The upper panel of Fig. 2 compares H–CO_2 total cross sections with those for O–CO_2 and C–CO_2 computed previously (Gacesa et al. 2020; Gacesa 2024). Even after reduced-mass scaling, these heavier projectiles produce cross sections that are substantially larger than the true H–CO_2 values. Using O–CO_2 (C–CO_2) as a proxy leads to typical scaling factors of ~ 12 (~ 9.5) and overestimation of the actual H–CO_2 total cross section by up to factors of ~ 45 (~ 30). Such discrepancies highlight the limitations of mass-scaling approaches frequently employed in atmospheric escape modelling. The scaled differential cross section fit of Lewkow & Kharchenko (2014) reproduces the general behaviour of the H–CO_2 total cross sections above ~ 1 eV, with deviations at the 10-15% level. At lower energies, however, where quantum effects are more pronounced, the deviation increases to $\sim 45\%$. Although the agreement at high energies is encouraging, the residual discrepancies remain larger than the isotopic H/D differences, reinforcing the need for dedicated quantum calculations for light-atom projectiles. This is expected because
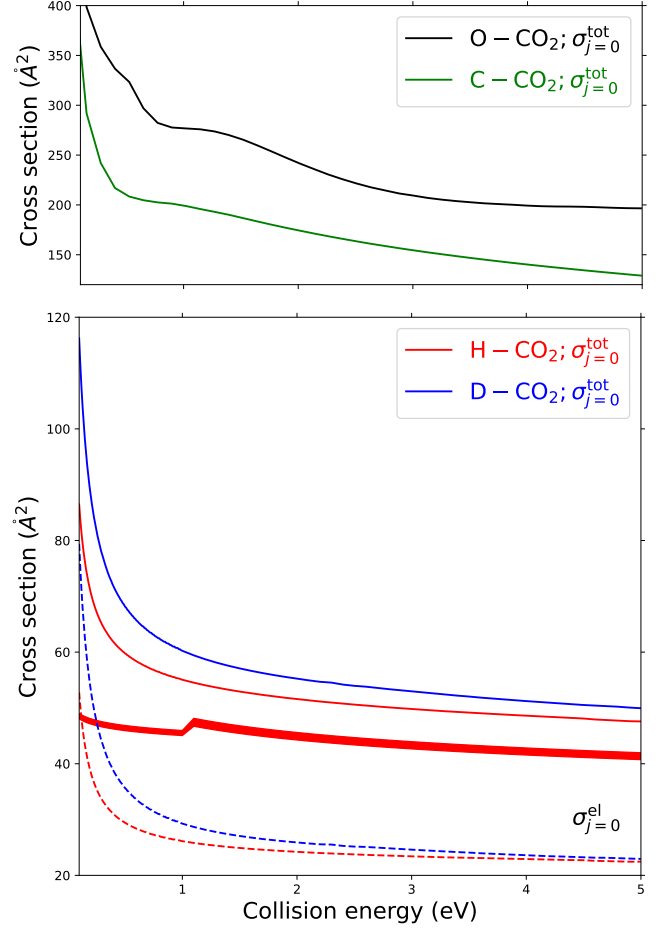

Figure 2. Total cross sections $\sigma_{j=0}^{tot}$ for CO_2 in collisions with H, D, O, and C as a function of collision energy. The O–CO_2 and C–CO_2 results are shown after reduced-mass scaling for comparison. The thick red line denotes the error margin of the H–CO_2 total cross sections from Lewkow & Kharchenko (2014). Dashed red and blue lines show the elastic contributions for H–CO_2 and D–CO_2, respectively.

the fitting approach does not explicitly resolve the full state-to-state rotational dynamics of the H–CO_2 system.

The left panel of Fig. 3 shows the angular dependence of the total and elastic differential cross sections for H–CO_2. Both exhibit strong forward scattering, with the forward peak contributing more than 90% of the integral cross section. This behaviour intensifies at higher collision energies, while the differential cross section decreases sharply with energy for scattering angles above $\sim 20°$. The elastic contribution falls rapidly with angle: it exceeds 80% below $2°$ but drops below $\sim 5\%$ at $180°$ across all energies considered.

The right panel of Fig. 3 shows the relative deviations in differential cross sections between H and D projectiles. As observed previously (Bop & Gacesa 2025b; Kumar et al. 2022; Zhang et al. 2009), the deviations are highly anisotropic and largest at small angles, where the differential cross section is most forward-peaked. For scattering angles below $\sim 2°$, fractional differences can reach two orders of magnitude at very small angles where the absolute cross section is already sharply peaked, whereas beyond this range the absolute deviations remain below $\sim 50\%$. This complex angular struc-
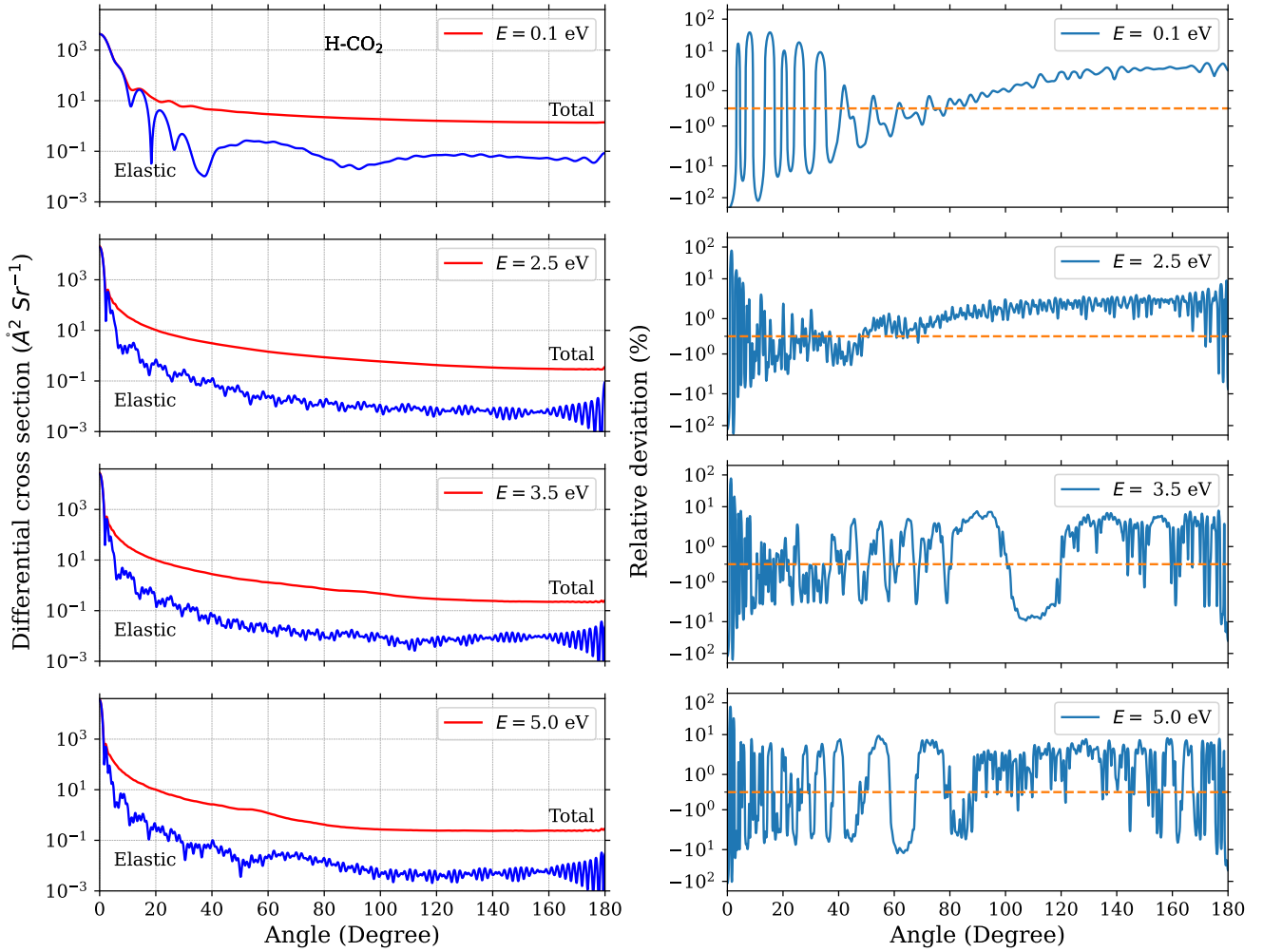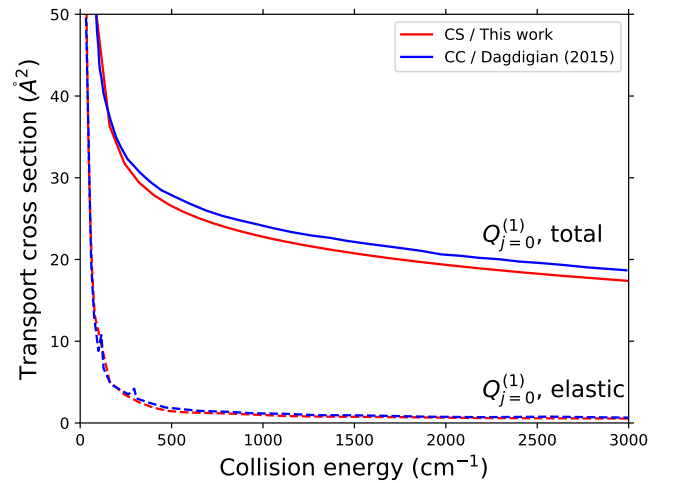
Figure 3. Angular dependence of H–CO₂ differential cross sections (left panel) and relative deviations upon H/D isotopic substitution (right panel) for selected collision energies. The horizontal line marks perfect agreement. Large relative deviations at very small angles occur in a strongly forward-peaked regime and should be interpreted together with the corresponding absolute cross sections.

ture demonstrates that isotopic substitution cannot be represented by a single mass-scaling correction.

3.2 Transport parameters

Figure 4 compares state-specific transport cross sections computed in this work using the CS approximation with the CC results of Dagdigian (2015). These cross sections weight collisions by $(1 - \cos\theta)$ and quantify the efficiency of momentum exchange rather than the overall scattering probability (Schunk & Nagy 2000). For escape and thermalisation modelling, σ_{mt} is the relevant quantity because it controls momentum loss per collision. [1] The two methods agree to within 7% across the full energy range. These small deviations likely reflect differences in numerical convergence, as both calculations employ the same potential energy surface.

Figure 4. Dependence of state-specific transport cross sections on collision energy for H–CO₂ $(j = 0)$. Dashed lines show the elastic contribution. Comparison between close-coupling and coupled-states calculations.

---

[1] The CC method, the most rigorous quantum approach, has itself been estimated to be accurate to within $\sim$10% when compared with available laboratory data at higher collision energies (Wiesenfeld et al. 2025).

For both isotopes, σ^{mt} is much smaller than the corresponding total and elastic cross sections across all energies, demonstrating that the scattering is strongly forward-peaked. As a result, individual H–CO$_2$ and D–CO$_2$ collisions rarely redirect the projectile by large angles, despite a high collision frequency. The small $\sigma_{\mathrm{mt}}/\sigma_{\mathrm{tot}}$ ratios imply long effective momentum-transfer mean free paths and inefficient collisional thermalisation, so hot H and D atoms retain a significant fraction of their incident momentum after each collision. As discussed in Sect. 4, this behaviour has direct implications for exobase structure and for the probability that suprathermal atoms escape or become quenched.

3.3 Maxwellian-averaged rate coefficients

For modelling applications, the relevant quantity is often the temperature-dependent rate coefficient rather than the energy-dependent cross section. We therefore compute Maxwellian-averaged momentum-transfer rate coefficients for thermal distributions of H and D atoms colliding with CO$_2$. The rate coefficient at temperature T is obtained by integrating the state-specific momentum-transfer cross section $\sigma^{\mathrm{mt}}(E)$ over a Maxwell–Boltzmann energy distribution:

$$k_{\mathrm{mt}}(T) = \langle \sigma^{\mathrm{mt}} v \rangle_T = \sqrt{\frac{8}{\pi\mu(k_{\mathrm{B}}T)^3}} \int_0^\infty \sigma^{\mathrm{mt}}(E) E e^{-E/k_{\mathrm{B}}T} dE, \quad (3)$$

where μ is the reduced mass of the collision system, k_{B} is Boltzmann's constant, E is the collision energy in the centre-of-mass frame, and $v = \sqrt{2E/\mu}$ is the relative speed. The integration is performed numerically using Simpson's rule, with $\sigma^{\mathrm{mt}}_{j=0}(E)$ taken from the $j=0$ state-specific results shown in Fig. 4. The same potential energy surface is used for both isotopes, so any differences in $k_{\mathrm{mt}}(T)$ arise solely from the different reduced masses and quantum scattering dynamics.

Table 1 lists $k_{\mathrm{mt}}(T)$ for both isotopes over the temperature range 100–5000 K, which spans conditions relevant to the Martian thermosphere and early planetary atmospheres. Over this range, the rate coefficients increase by approximately a factor of 7, reflecting the energy dependence of $\sigma_{\mathrm{mt}}(E)$. The isotopic ratio $k_{\mathrm{D}}/k_{\mathrm{H}}$ is approximately 0.6 across the temperature range, indicating that deuterium atoms transfer about 40% less momentum per collision than hydrogen atoms at comparable temperatures. This mass dependence is consistent with expectations for light-atom scattering where the reduced mass affects both the de Broglie wavelength and the classical momentum exchange.

Table 1. Maxwellian-averaged momentum-transfer rate coefficients $k_{\mathrm{mt}}(T)$ for H/D–CO$_2$ collisions. The final column gives the isotopic ratio $k_{\mathrm{D}}(T)/k_{\mathrm{H}}(T)$.

T (K)	k_{H} (cm³ s⁻¹)	k_{D} (cm³ s⁻¹)	$k_{\mathrm{D}}/k_{\mathrm{H}}$
100	3.53×10^{-11}	2.08×10^{-11}	0.589
200	2.36×10^{-11}	1.46×10^{-11}	0.618
300	1.84×10^{-11}	1.14×10^{-11}	0.619
500	1.38×10^{-11}	8.41×10^{-12}	0.610
1000	1.01×10^{-11}	5.97×10^{-12}	0.590
2000	8.35×10^{-12}	4.81×10^{-12}	0.576
3000	7.77×10^{-12}	4.44×10^{-12}	0.571
5000	7.21×10^{-12}	4.09×10^{-12}	0.568
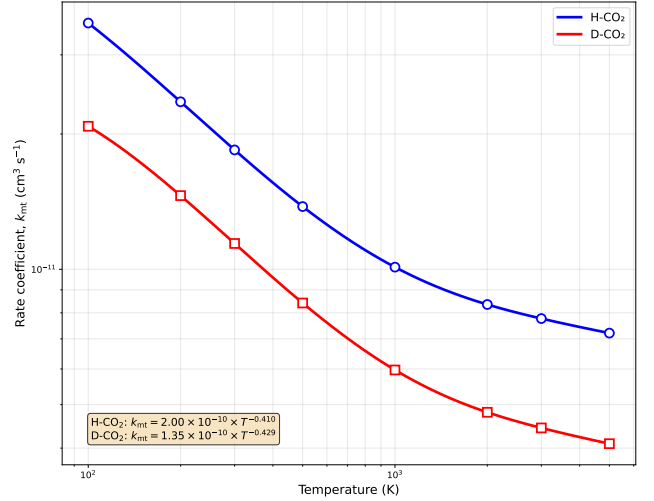
Figure 5. Maxwellian-averaged momentum-transfer rate coefficients $k_{\mathrm{mt}}(T)$ for H–CO$_2$ (blue circles and line) and D–CO$_2$ (red squares and line) collisions. Solid curves show the smoothly interpolated values, while symbols mark the temperatures listed in Table 1. The behaviour is well approximated by power laws (dashed lines) of the form $k(T) = AT^B$ with $A_{\mathrm{H}} = 2.00 \times 10^{-10}$ cm³ s⁻¹, $B_{\mathrm{H}} = -0.410$ for H–CO$_2$ and $A_{\mathrm{D}} = 1.35 \times 10^{-10}$ cm³ s⁻¹, $B_{\mathrm{D}} = -0.429$ for D–CO$_2$.

Figure 5 displays the temperature dependence of $k_{\mathrm{mt}}(T)$ for both isotopes. The curves are well described by simple power-law fits, $k(T) = AT^B$, with the parameters given in the caption. These fits provide a convenient analytic representation for implementation in atmospheric models where a full integration of Eq. (3) is impractical.

The momentum-transfer rate coefficients presented here, $k_{\mathrm{H}}(300\ \mathrm{K}) = 1.84 \times 10^{-11}$ cm³ s⁻¹ and $k_{\mathrm{D}}(300\ \mathrm{K}) = 1.14 \times 10^{-11}$ cm³ s⁻¹, are consistent in magnitude with values for similar light-atom–molecule systems such as H–N$_2$ (Schunk & Nagy 2000). However, they differ significantly from values sometimes adopted in atmospheric models that employ simplified scaling approaches. For comparison, mass-scaling from O–CO$_2$ cross sections (Gacesa et al. 2020) would yield $k_{\mathrm{H}}(300\ \mathrm{K}) \sim 3 \times 10^{-10}$ cm³ s⁻¹, approximately 16 times larger than our quantum-mechanical result. This discrepancy arises because forward-peaked scattering characteristic of light-atom collisions yields much smaller momentum-transfer cross sections than would be predicted by isotropic or hard-sphere models.

4 CONCLUSION

We have computed comprehensive state-to-state, total, and transport cross sections for rotationally elastic and inelastic collisions between hot hydrogen atoms and CO$_2$ using a time-independent, j_z-conserving coupled-states quantum mechanical approach. The calculations span collision energies relevant to both thermal and non-thermal escape processes in CO$_2$-rich planetary atmospheres, including the Martian upper atmosphere.

For CO$_2$ in its ground rotational state, inelastic cross sections decrease rapidly with increasing final rotational quantum number j', with transitions beyond $\Delta j \gtrsim 140$ contribut-

ing negligibly to the total. A systematic comparison of H–CO_2 and D–CO_2 collisions shows that isotopic differences are strongly energy dependent: D–CO_2 cross sections exceed H–CO_2 values by up to ∼35% at $E < 0.1$ eV, while differences fall below ∼9% at higher energies. These results demonstrate that isotopic substitution cannot be represented by a uniform scaling factor when accurate escape modelling is required.

Comparisons with previously used surrogate systems show that reduced-mass scaling based on O–CO_2 and C–CO_2 collisions substantially overestimates H–CO_2 cross sections, by factors of up to ∼45 and ∼30, respectively. Empirical fits reproduce the general high-energy behaviour but underestimate the low-energy regime by as much as ∼45%. Together, these findings underscore the limitations of mass-scaling and fitting approaches widely employed in escape studies, and highlight the importance of system-specific quantum calculations for light-atom collisions with polyatomic targets.

4.1 Implications for atmospheric escape

The cross sections presented here provide the first quantum-mechanical replacement for the simplified collisional parameters that have been used since the foundational escape models of Hunten (1973) and Schunk & Nagy (1980). Our results show that these classical approximations overestimate H–CO_2 total cross sections by factors of 30–45 and rate coefficients by approximately $16\times$. This revision has direct implications for modelling early Earth hydrogen escape, where sustained loss is required to explain noble-gas isotopic constraints (Zahnle et al. 2019). The warmer thermospheres implied by our reduced cooling efficiencies could help reconcile escape models with geochemical evidence, demonstrating how microscopic quantum scattering physics can reshape macroscopic planetary evolution scenarios.

For thermal (Jeans) escape, the relevant quantity is the momentum-transfer cross section σ_{mt}. In a simple isothermal exobase formulation, if a mass-scaled σ_{mt} exceeds the true H–CO_2 value by a factor f, the exobase altitude shifts by $\Delta z_{exo} \simeq H \ln f$. Because commonly used mass-scaled values can overestimate the true H–CO_2 cross section by up to an order of magnitude at sub-eV energies, exobase shifts of order ∼10–20 km are plausible in such simplified models. Since the Jeans flux depends exponentially on the escape parameter, even modest changes in exobase altitude and temperature can lead to order-unity changes in the thermal escape rate of hydrogen. Similar considerations apply to deuterium, with the added complexity that its thermalisation efficiency differs from that of H in a non-uniform, energy-dependent manner.

For non-thermal escape, the connection to the cross sections is more direct. Photochemically produced hot H and D atoms undergo only a small number of collisions while traversing the upper thermosphere, so differences of a factor of a few between true and mass-scaled total or momentum-transfer cross sections translate directly into comparable changes in the number of collisions experienced by a typical suprathermal atom. Escape probabilities in Monte Carlo and test-particle models are therefore expected to be systematically modified when the present state-resolved cross sections are implemented. Because the isotopic differences in the H–CO_2 and D–CO_2 cross sections are energy dependent, the resulting D/H fractionation in escape is likewise expected to differ from current estimates based on simplified scaling assumptions.

Beyond Mars, the present cross sections are also relevant for CO_2 cooling and hydrogen escape in hydrogen-rich upper atmospheres. Related collisional regimes are also encountered in cometary comae, where CO_2 is a major volatile and photodissociation produces suprathermal H atoms in a low-collision environment (Bockelée-Morvan et al. 2004; Combi et al. 2004), and in the present-day terrestrial thermosphere, where H–CO_2 energy transfer contributes to CO_2 cooling despite CO_2 being a minor constituent (Roble & Dickinson 1989; Mlynczak et al. 2010).

In early Earth and early Venus thermospheres, collisional energy transfer between H and CO_2 regulates the efficiency of 15 μm CO_2 cooling, which in turn governs thermospheric temperature structure and hydrogen loss. Such processes are central to reconciling noble-gas constraints on early Earth atmospheric evolution, where sustained hydrogen escape is required to explain xenon isotopic fractionation and long-term volatile loss (Zahnle et al. 2019), with implications for CO_2 cooling efficiency in hydrogen-rich atmospheres (Harman et al. 2018). The cross sections presented here also provide updated microscopic inputs for revisiting scenarios of hydrodynamic escape and noble gas fractionation (Zahnle & Kasting 1986; Zahnle et al. 1990), where accurate H–CO_2 collision rates are essential for determining diffusion coefficients and mass fractionation patterns during the 'flight of the nobility' from early planetary atmospheres.

Our calculated momentum-transfer rate coefficients (Table 1) are approximately 16 times smaller than would be obtained by mass-scaling from O–CO_2 collisions (Gacesa et al. 2020), implying that H–CO_2 energy transfer in hydrogen-rich regimes may have been less efficient than previously estimated. This would lead to reduced CO_2 cooling efficiency, potentially resulting in warmer upper atmospheres and enhanced thermal escape rates — a factor that could help reconcile models of early atmospheric evolution with noble-gas isotopic constraints. A full assessment of these effects requires coupled thermosphere–ionosphere modelling and is left for future work.

More broadly, recent progress in planetary escape modelling has shifted major uncertainties from global drivers such as solar EUV flux toward the microscopic physics of collisional energy and momentum transfer in the upper atmosphere. The cross sections presented here therefore provide essential input data for a wide class of escape models, reducing reliance on mass-scaled or surrogate collision systems and enabling more physically grounded predictions of atmospheric evolution in CO_2-rich planetary and exoplanetary environments.

CONFLICTS OF INTEREST

There are no conflicts to declare.

DATA AVAILABILITY

The cross sections and rate coefficients presented in this paper are available as electronic supplementary material and have been deposited in the Zenodo repository at https://doi.org/10.5281/zenodo.17549249 (Bop & Gacesa 2025a).

REFERENCES

Alexander M. H., 1977, The Journal of Chemical Physics, 67, 2703
Alexander M. H., Manolopoulos D. E., 1987, The Journal of chemical physics, 86, 2044
Amerstorfer U. V., et al., 2017, Journal of Geophysical Research: Planets, 122, 1321
Balakrishnan N., 2004, The Journal of chemical physics, 121, 6346
Bockelée-Morvan D., Crovisier J., Mumma M. J., Weaver H. A., 2004, in Festou M. C., Keller H. U., Weaver H. A., eds, , Comets II. University of Arizona Press, pp 391–423
Bop C. T., Gacesa M., 2025a, Superthermal kinetic energy transfer via CO2 collisions with H and D: elastic and inelastic cross sections, doi:10.5281/zenodo.17549248, https://doi.org/10.5281/zenodo.17549248
Bop C. T., Gacesa M., 2025b, Monthly Notices of the Royal Astronomical Society: Letters, p. slaf092
Bop C., Lique F., 2023, The Journal of Chemical Physics, 158, 074304
Cadieux C., et al., 2024, The Astrophysical Journal Letters, 960, L3
Cangi E. M., Chaffin M. S., Stewart I., McClintock W., Brain D., Jakosky B. M., 2023, arXiv e-prints
Chaffin M. S., Chaufray J.-Y., Stewart I., Montmessin F., Schneider N. M., Clarke J. T., 2014, Geophysical Research Letters, 41, 314
Chaufray J.-Y., et al., 2024, Icarus, 418, 116152
Clarke J. T., Mayyasi M., Bhattacharyya D., Chaufray J., et al., 2024, Science Advances, 10
Combi M. R., Harris W. M., Smyth W. H., 2004, in Festou M. C., Keller H. U., Weaver H. A., eds, , Comets II. University of Arizona Press, pp 523–552
Dagdigian P. J., 2015, The Journal of Chemical Physics, 143
Feaga L., A'Hearn M., Sunshine J., Groussin O., Farnham T., 2007, Icarus, 191, 134
Fox J. L., 2015, Icarus, 252, 366
Fox J. L., Hac A., 2009, Icarus, 204, 527
Gacesa M., 2024, Monthly Notices of the Royal Astronomical Society, 528, 2621
Gacesa M., Kharchenko V., 2014, J. Chem. Phys., 141, 164324
Gacesa M., Lewkow N., Kharchenko V., 2017, Icarus, 284, 90
Gacesa M., Lillis R. J., Zahnle K. J., 2020, Monthly Notices of the Royal Astronomical Society, 491, 5650
Garton D. J., Minton T. K., Maiti B., Troya D., Schatz G. C., 2003, J. Chem. Phys., 118, 1585
Gong Y., et al., 2025, Astronomy & Astrophysics, 696, A31
Gregory B. S., Elliott R. D., Deighan J., Gröller H., Chaffin M. S., 2023a, Journal of Geophysical Research: Planets, 128, e2022JE007576
Gregory B. S., Chaffin M. S., Elliott R. D., Deighan J., Gröller H., Cangi E., 2023b, Journal of Geophysical Research: Planets, 128, e2023JE007802
Harman C. E., Felton R., Hu R., Domagal-Goldman S. D., Segura A., Tian F., Kasting J. F., 2018, ApJ, 866, 56
Hunten D. M., 1973, Journal of Atmospheric Sciences, 30, 1481
Hutson J., Green S., 1994, Collaborative computational project
Jakosky B. M., et al., 2017, Science, 355, 1408
Jakosky B., et al., 2018, Icarus, 315, 146
Kumar S., Gacesa M., Khalil M. S., Al Ghaferi A., El-Kork N., 2022, Monthly Notices of the Royal Astronomical Society, 519, 1253
Lewkow N., Kharchenko V., 2014, The Astrophysical Journal, 790, 98
Lillis R. J., Brain D., Jakosky B., et al., 2017, Journal of Geophysical Research: Space Physics, 122, 3815
Limaye S. S., Mogul R., Smith D. J., Ansari A. H., Słowik G. P., Vaishampayan P., 2018, Astrobiology, 18, 1181
Madhusudhan N., 2012, The Astrophysical Journal, 758, 36
Mayyasi M., Clarke J. T., Chaufray J.-Y., Bhattacharyya D., et al., 2023, Icarus, 398, 115527
McGuire P., Kouri D. J., 1974, The Journal of Chemical Physics, 60, 2488
Mlynczak M. G., Hunt L. A., Marshall B. T., et al., 2010, Geophysical Research Letters, 37, L05103
Ndaw D., Dieye G., Faye N. B., 2021, Monthly Notices of the Royal Astronomical Society, 503, 5976
Roble R. G., Dickinson R. E., 1989, Journal of Geophysical Research, 94, 14463
Schunk R., Nagy A., 1980, Reviews of Geophysics, 18, 813
Schunk R. W., Nagy A. F., 2000, Ionospheres: Physics, plasma physics, and chemistry. Cambridge university press
Susarla R., et al., 2024, Journal of Geophysical Research: Space Physics, 129, e2024JA032525
Thomas T. B., Hu R., Lo D. Y., 2023, Planet. Sci. J., 4, 41
Turbet M., et al., 2018, Astronomy & Astrophysics, 612, A86
Wiesenfeld L., Niraula P., de Wit J., Jaïdane N., Gordon I. E., Hargreaves R. J., 2025, The Astrophysical Journal, 981, 148
Zahnle K. J., Kasting J. F., 1986, Icarus, 68, 462
Zahnle K., Kasting J. F., Pollack J. B., 1990, Icarus, 84, 502
Zahnle K. J., Gacesa M., Catling D. C., 2019, Geochimica et Cosmochimica Acta, 244, 56
Zhang P., Kharchenko V., Jamieson M., Dalgarno A., 2009, Journal of Geophysical Research: Space Physics, 114

This paper has been typeset from a TEX/LATEX file prepared by the author.